Comparison of single-ion-conductor block-copolymer electrolytes with Polystyrene- TFSI and Polymethacrylate- TFSI structural blocks

Didier Devaux, Livie Liénafa, Emmanuel Beaudoin, Sébastien Maria, Trang N.T. Phan, Didier Gigmes, Emmanuelle Giroud, Patrick Davidson, Renaud Bouchet

Electrochimica Acta 269 (2018) 250–261

Contents lists available at ScienceDirect

Electrochimica Acta

journal homepage: www.elsevier.com/locate/electacta

Comparison of single-ion-conductor block-copolymer electrolytes with Polystyrene-*TFSI* and Polymethacrylate-*TFSI* structural blocks

Didier Devaux [a], Livie Liénafa [b], Emmanuel Beaudoin [c], Sébastien Maria [b], Trang N.T. Phan [b], Didier Gigmes [b], Emmanuelle Giroud [a], Patrick Davidson [c], Renaud Bouchet [a, *]

[a] Univ. Grenoble Alpes, CNRS, Institute of Engineering Univ. Grenoble Alpes (Grenoble INP), LEPMI, 38000 Grenoble, France
[b] Aix-Marseille Univ., CNRS, ICR, UMR 7273, 13397 Marseille, France
[c] Laboratoire de Physique des Solides, CNRS, UMR 8502, Université Paris-Sud, Université Paris-Saclay, 91405 Orsay Cedex, France

ARTICLE INFO

Article history:
Received 19 November 2017
Received in revised form
22 February 2018
Accepted 25 February 2018
Available online 2 March 2018

Keywords:
Single-ion conductor
Polymer electrolyte
Lithium battery
PEO
VTF

ABSTRACT

A new family of single-ion-conductor block-copolymer electrolytes (BCEs), comprising poly(ethylene oxide) (PEO) as conducting block and poly(styrene sulfonyl(trifluoromethanesulfonyl) imide of lithium) (PS*TFSI*) as structural block, was developed recently. To evaluate the influence of the structural blockon the physico-chemical and electrochemical properties, we compare two single-ion-conductor BCE families with structural blocks made of either PS*TFSI* or poly(3-sulfonyl(trifluoromethanesulfonyl) imide propyl methacrylate of lithium) (PMA*TFSI*). Small-angle X-ray scattering revealed that at temperatures lower than the PEO block melting temperature, the morphology of both families is lamellar whereas, at higher temperatures, the electrolytes are in a disordered state. Both electrolyte families present an ionic conductivity maximum for some weight fraction of the structural block (w_{BTFSI}), named B*TFSI*. For $w_{BTFSI} >$ 0.17, the ionic conductivity of the PMA*TFSI*-based electrolytes is larger than that of the PS*TFSI*-based electrolytes by at least a factor of two. Based on a detailed transport analysis, we show that the strong increase of the glass transition temperature is the main factor limiting the ionic conductivity. We also interpret the conductivity maximum of the PS*TFSI*-based electrolytes by a limitation in available free charges for $w_{PSTFSI} > 0.17$ while the polymer dynamics slows down. The optimization of the ionic transport in this type of single-ion-conductor BCE requires promoting the compatibility of the Li^+-bearing structural block with the conducting block.

1. Introduction

The increasing demand in reliable renewable energy, such as photovoltaic and wind power, implies the development of low cost and safe high energy density secondary batteries [1–3]. Lithium (Li) ion batteries are not adequate for this purpose because of their high price and their flammable liquid electrolyte which raises strong safety issues [4,5]. Replacing conventional liquid electrolytes by an inherently safe solid polymer electrolyte opened the path of high energy density Li metal batteries [6]. In this context, poly(ethylene oxide) (PEO) is the most studied polymer as it dissociates and complexes Li salts, such as lithium bis(trifluoromethanesulfonyl) imide (LiTFSI) [7,8]. Ionic transport in PEO depends on the backbone flexibility and occurs mostly in its amorphous phase [9,10]. Thus, Li metal polymer batteries have to operate at a temperature (T) above the PEO melting temperature (T_m), generally above 70 °C. However, in this temperature range, PEO polymers are viscoelastic liquids which do not prevent the growth of Li-metal dendrites upon cycling [11,12].

One solution to combine good ionic conductivity and mechanical resistance towards Li dendrite growth is to use nanostructured solid block copolymer electrolytes (BCEs) [13–16]. Block copolymers are of interest as they can self-assemble in ordered structures at nanoscopic scales [17,18]. One block (A) is a PEO-based polymer doped with a Li salt to ensure ionic conductivity whereas the other block (B) brings different functionalities, depending on its structure, such as mechanical strength. For example, the B block

* Corresponding author.
E-mail address: Renaud.Bouchet@lepmi.grenoble-inp.fr (R. Bouchet).

https://doi.org/10.1016/j.electacta.2018.02.142
0013-4686/

can be made of a polymer with high glass-transition temperature (T_g), such as polystyrene (PS) [19,20] or poly(methyl methacrylate) [21–23]. Despite interesting results achieved so far in terms of ionic conductivity, mechanical properties, or battery performance, the use of block copolymer electrolytes is still restricted by their inability to prevent dendrite growth [24–26] and by their low lithium transference number [20]. Indeed, only a small fraction of the electric current, usually 20%, is driven by the Li^+ ions, which implies limited battery power performance and enhanced Li dendrite growth [27,28].

To overcome these limitations, polyanionic block copolymers have been used to produce single-ion-conductor electrolytes [13,29]. Based on these studies, we have previously shown that BCEs comprising a polyanionic B block exhibit enhanced performance compared to conventional block copolymer electrolytes [30]. These single-ion-conductor electrolytes are made of poly(-styrene sulfonyl(trifluoromethanesulfonyl)imide of lithium) (PS*TFSI*) as outer blocks associated with a central PEO block. They have both an ionic conductivity of 1.3×10^{-5} S/cm at 60 °C and good mechanical properties. Their electrochemical window of stability extends to 4.5 V vs. Li^+/Li and their application in Li metal batteries exhibits remarkable capacity retention, notably at 60 °C. Interestingly, Balsara and coworkers, using PS*TFSI*-PEO diblock copolymers, showed that the crystallinity of the PEO domains determines the morphology of the nanostructured electrolytes below the melting temperature of PEO ($T_{m,PEO}$) while, for $T > T_{m,PEO}$, the material is in a disordered state, which allows reaching high ionic conductivity [31,32]. These studies launched a new concept of single-ion-conductor polymer electrolytes in which one or several polymer segments are functionalized with a Li^+-bearing structural block [33–40].

Here, we report on the physico-chemical and electrochemical characterizations of single-ion-conductor BAB triblock copolymer electrolytes with a central PEO block and variable nature of the structural block to optimize the ionic conductivity. The outer B blocks have a polyanionic structure, where the $TFSI^-$ anions are grafted onto the polymer backbone composed of either polystyrene (PS*TFSI*) or poly(methyl methacrylate) (PMA*TFSI*). One of the very interesting features of these polymers is that they are soluble in water, which opens the way to simple large-scale electrolyte film formulation. The thermal, structural, and electrochemical properties, as well as the ionic conductivity and transference number of the PMA*TFSI*-based electrolytes are reported and discussed here in comparison with those of the corresponding PS*TFSI*-based electrolytes. In addition, by modeling the lithium conductivity in the framework of free-volume theory, different transport limitations arising from available free charges or glass-transition temperature effects are shown.

2. Experimental

2.1. Materials

Sodium 4-styrenesulfonate (SSNa, >90%), potassium 3-sulfopropyl methacrylate (MASPK, 98%), 480 g/mol poly(ethylene glycol) methyl ether acrylate (APEG), oxalyl chloride (>99%), triethylamine (TEA, >99%), anhydrous acetonitrile and anhydrous *N,N*-dimethylformamide were purchased from Aldrich. Trifluoromethanesulfonamide (TFSA) was ordered from TCI Europe. *N*-(2-methylpropyl)-*N*-(1-diethylphosphono-2,2-dimethylpropyl)-*N*-oxyl (SG1) (85%) and alkoxyamine based on SG1 derived from methacrylic acid (MAMA-SG1, >99%, trade name BlocBuilder MA) were kindly supplied by Arkema. All the above commercial chemicals were used as received.

2.2. Monomer synthesis

The chemical structures of two monomers used in this work to synthesize polyanionic triblock copolymers are shown in Fig. 1. The monomers are 4-sulfonyl potassium (trifluoromethylsulfonyl) imide styrene (K-S*TFSI*) and 3-sulfonyl potassium (trifluoromethylsulfonyl)imide propyl methacrylate (K-MA*TFSI*). K-S*TFSI* was prepared according to literature [41]. The synthesis of K-MA*TFSI* is inspired from previous works [38,42] with some modification [43].

2.3. Block copolymer synthesis

Hereafter, the single-ion-conductor BAB triblock copolymers are referred to PS*TFSI*-*b*-PEO-*b*-PS*TFSI* and PMA*TFSI*-*b*-PEO-*b*-PMA*TFSI* where PS*TFSI* and PMA*TFSI* are poly(styrene sulfonyl(trifluoromethanesulfonyl)imide of lithium), and poly(3-sulfonyl(trifluoromethanesulfonyl) imide propyl methacrylate of lithium), respectively. The chemical structures of the monomers and block copolymers are shown in Fig. 1. Triblock copolymers were synthesized in three steps. Firstly, α,ω-dihydroxyl-PEO was reacted with acryloyl chloride to form the corresponding PEO-diacrylate. Secondly, PEO-based macroalkoxyamine (PEO(MAMA-SG1)$_2$) was synthesized by reacting PEO-diacrylate and MAMA-SG1. Finally, the last step was nitroxide-mediated polymerization (NMP), in water at 100 °C, of anionic monomer using PEO-based macroalkoxyamine as initiator. For the methacrylate monomer MA*TFSI*, the NMP synthesis route requires its copolymerization with a small amount of a given co-monomer to ensure polymerization control. The different co-monomers employed with MA*TFSI* were either APEG or S*TFSI* to produce random copolymer B blocks. Elimination of unreacted monomer and K^+ exchange by Li^+ were performed by successive dialyses against $LiClO_4$ solution and distilled water to produce pure Li^+ single-ion-conductor BAB triblock copolymers.

2.4. Macromolecular characterization

Monomer conversion, copolymer composition, and total number-average molecular weight (M_n) were determined from ^{1}H NMR spectra recorded on a Bruker Avance 400 MHz spectrometer, using D_2O as solvent (the ^{1}H NMR spectra of chosen BCEs are given in Supplementary Figs. S1–S4). Size-exclusion chromatography (SEC) was performed on a Waters 600 chromatography system equipped with a Waters Refractive Index Detector and two MCX columns (PSS) mounted in series and thermostated at 50 °C. The eluent was a 50/50 (vol/vol) mixture of a Na_2HPO_4 (0.15 wt%) aqueous solution and acetonitrile at a flow rate of 1 mL/min. Relative calibration was conducted with standard PEO samples. The characteristics of the single-ion-conductor electrolytes are listed in Table 1 along with M_n, and the weight fraction of PEO (w_{EO}), B block (w_B), and co-monomer (w_C) within the B block. For clarity, the electrolytes are labeled "B*TFSI*_*Y*" hereafter, according to the nature of the B block (PS*TFSI* or PMA*TFSI*) and to the weight fraction (*Y*) of TFSI-grafted-B blocks (w_{BTFSI}) in percent. For example, PS*TFSI*_9 refers to the PS*TFSI*-*b*-PEO-*b*-PS*TFSI* electrolyte with a central 35 kg/mol PEO block and a PS*TFSI* weight fraction (w_{PSTFSI}) of 0.09.

2.5. Electrolyte preparation

Solvent casting was used to produce solid electrolyte thin films. After synthesis, the single-ion-conductor BCE was dissolved in water at 10 wt% concentration. After mechanical homogenization, the solution was cast on a polypropylene substrate and evaporated slowly at room temperature during 24 h. The resulting film was further dried by annealing in a vacuum oven during 24 h at 50 °C,

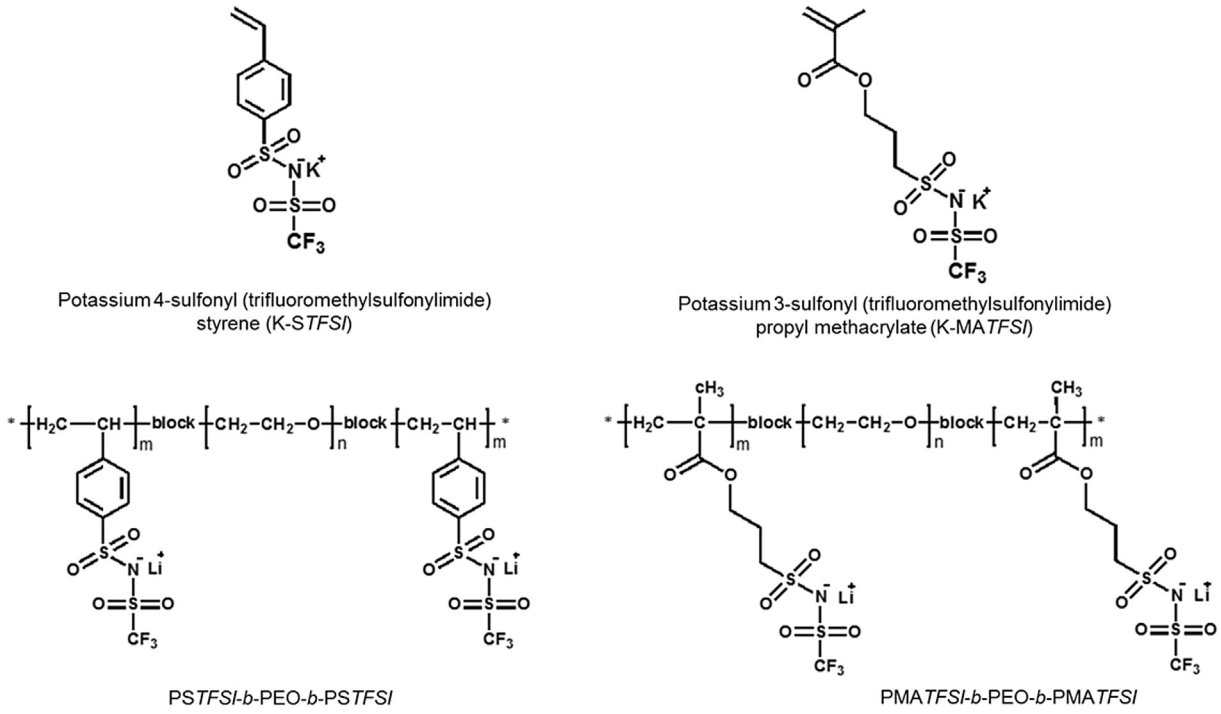

Fig. 1. Chemical structure of the anionic monomers K-*STFSI* and K-MA*TFSI*, and the corresponding B*TFSI*-PEO-B*TFSI* triblock copolymers with a central 35 kg/mol PEO block.

Table 1
Characteristics of the single-ion BCEs with the total molecular weight (M_n), and the weight fraction of PEO (w_{EO}), B block (w_B), co-monomer (w_C), B*TFSI* (w_{BTFSI}). The domain spacing (d) obtained by SAXS measurements and the transference number (t^+) for some of the BCEs are also included.

	comonomer	M_n[a] (kg/mol)	w_{EO}	w_B	w_C (c = comonomer)	w_{BTFSI}	d (nm)	t^+ (at 90 °C)
PS*TFSI*_9		39	0.91	0.09	–	0.09	32	0.84 ± 0.03
PS*TFSI*_17		42	0.83	0.17	–	0.17	29	0.90 ± 0.03
PS*TFSI*_18		43	0.82	0.18	–	0.18	–	0.87 ± 0.03
PS*TFSI*_21		45	0.79	0.21	–	0.21	–	0.90 ± 0.02
PS*TFSI*_23		45	0.77	0.23	–	0.23	29	–
PS*TFSI*_25		47	0.75	0.25	–	0.25	–	–
PS*TFSI*_28		49	0.72	0.28	–	0.28	33	–
PS*TFSI*_31		51	0.69	0.31	–	0.31	–	–
PS*TFSI*_43		61	0.57	0.43	–	0.43	–	–
PMA*TFSI*_6	APEG	39	0.89	0.11	0.05	0.06	27	0.85 ± 0.05
PMA*TFSI*_9	APEG	39	0.89	0.11	0.02	0.09	–	–
PMA*TFSI*_13	S*TFSI*	40	0.87	0.13	0.01	0.13	–	0.82 ± 0.04
PMA*TFSI*_17	APEG	44	0.79	0.21	0.04	0.17	27	0.80 ± 0.04
PMA*TFSI*_21	APEG	47	0.75	0.25	0.04	0.21	–	0.83 ± 0.05
PMA*TFSI*_27	APEG	54	0.65	0.35	0.08	0.27	32	0.81 ± 0.03
PMA*TFSI*_30	S*TFSI*	50	0.70	0.30	0.04	0.30	30	0.88 ± 0.03
PMA*TFSI*_43	APEG	73	0.48	0.52	0.09	0.43	–	0.89 ± 0.03

[a] Determined by proton NMR. Knowing the Mn of commercial PEO, the Mn of the B block was calculated by comparing the integrals of the PSTFSI phenyl protons signals and those of the PEO protons signals. For PMATFSI based materials, the integrals of $-OCH_2-$ protons were considered.

and was finally placed in an argon-filled glove box (<1 ppm H_2O, O_2, Jacomex) for at least a week before any experiment. The amount of water in the dried films, measured by Karl-Fisher (TitroLine 7500 KF trace from SI Analytics) method, was around 20 ppm. On average, the final solid electrolyte film thickness was 50 ± 10 μm, with the symbol ± used hereafter to denote the standard deviation.

2.6. Thermodynamic characterization

Differential Scanning Calorimetry (DSC) was performed with a DSC 2920 from TA Instruments under a constant flow of inert gas (nitrogen) between −60 and 120 °C at 5 °C/min. To obtain the same thermal history for all the samples, a first heat/cool cycle was performed before running a second cycle [44]. From the PEO endothermic peak of the second cycle, the PEO melting temperature ($T_{m,PEO}$) was determined from the intersection of the base line with the tangent at the peak maximum (melting onset). The PEO degree of crystallinity ($X_{c,PEO}$) was deduced from the melting enthalpy ($\Delta H_{m,PEO}$, determined by peak integration) and w_{EO} (Table 1), according to:

$$X_{c,PEO} = \frac{\Delta H_{m,PEO}}{w_{EO} \cdot \Delta H^0_{m,PEO}} \quad (1)$$

where $\Delta H^0_{m,PEO}$ is the melting enthalpy, 195 J/g, of a 100% crystalline PEO [45]. The glass transition temperature of the PEO block could not be properly measured because it is mostly crystalline [32].

2.7. Thermal stability

The electrolyte thermal stability was investigated by thermogravimetric analysis (TGA) on a TGA Q500 from TA instruments between 30 and 500 °C at 10 °C/min under a constant flow of inert argon gas after thermal equilibration for an hour at 30 °C. The samples were mounted onto an alumina pan inside the glove box and transferred to the apparatus via hermetic vials. The onset temperature of electrolyte degradation (T_d) was determined from the intersection of the baseline with the tangent of the weight loss curve.

2.8. Small-angle and wide-angle X-ray scattering

The organization of the single-ion-conductor BCEs was investigated by small-angle X-ray scattering (SAXS) and wide-angle X-ray scattering (WAXS). The setup equipped with a rotating copper anode generator (wavelength $\lambda = 0.154$ nm) and an Osmic multilayered optics has been described previously [46]. The sample was brought at the desired temperature in a Linkam heating plate (equipped with Mylar windows whose signal was subtracted) with a Linkam TMS92 control unit. The temperature ranged from 30 to 90 °C, and the heating rate was 1 °C/min. The sample-to-detector distance was 1.17 m for SAXS and 0.05 m for WAXS. The scattered X-rays were detected by a CCD Princeton camera. Exposure times typically ranged from 5 to 15 min for SAXS and from 1 to 2 min for WAXS. Data processing (dark current subtraction, flat-field correction, and normalization) was performed using homemade software. The accessible range of scattering vector modulus q ($q = (4\pi\sin\theta)/\lambda$, where 2θ is the scattering angle) was $0.08 < q < 1.00\ \text{nm}^{-1}$ for SAXS and the range of scattering angle was $5° < 2\theta < 45°$ for WAXS. 1-dimensional $I(q)$ curves of the scattered intensity versus q for SAXS or $I(2\theta)$ versus 2θ for WAXS were obtained by angular averaging of the scattering patterns. Calibration of WAXS scattering angle was performed using a quartz sample.

At small angles, the maximum of a 1st order scattering peak, at a scattering vector modulus q^*, provides the domain spacing (d) by using the simple formula:

$$\boldsymbol{d} = 2\,\pi/\boldsymbol{q}^* \tag{2}$$

The ratio between q^* and the scattering-vector moduli of higher-order peaks were used to determine the phase symmetry (e.g. integer multiples $q/q^* = 2, 3, \ldots$indicate a lamellar morphology).

2.9. Cell assemblies and testing

Lithium symmetric cells were assembled in an argon-filled glove box using a homemade laminating machine set to operate at 80 °C and 3 bars. Each cell consisted of the superposition of the electrolyte film and a 23 μm thick polyethylene spacer defining the active surface area (S) placed between two 100 μm thick Li metal disks with copper grid (Goodfellow) current collector tabs [47]. At each step of the lamination process, the electrolyte thickness (l) was monitored using a micrometer (Mitutoyo) with a ±1 μm precision. After assembly, the cell was sealed in an airtight pouch bag (Protective Packaging Ltd), removed from the glove box, placed in a climatic chamber (Vöetsch), and connected to a Solartron 1260 frequency analyzer. For ionic conductivity (σ) measurement, AC impedance spectroscopy was performed using a voltage excitation signal of 10 mV (40 mV was also used at low temperatures) in a frequency range between 10^7 and 1 Hz. The Li symmetric cells were first heated from 30 to 100 °C by steps of 10 °C, followed by a cooling scan from 85 to 45 °C every 10 °C, before returning to 30 °C; then, a final heating scan by steps of 10 °C was carried out up to 100 °C. A stabilization time of one hour was used at each step and the reproducibility of the data during heating and cooling was systematically checked. For all the electrolytes, the experimental data extracted from the cooling and heating scans were similar, demonstrating the stability of the polymers. Only data recorded during the last cooling/heating scans are presented. The Li^+ transference number (t^+) was determined at 90 °C by AC impedance spectroscopy down to 10^{-4} Hz using a Solartron 1260 (Ametek). A typical impedance spectrum of the PMA*TFSI*_27 electrolyte is shown in Fig. S5. The impedance spectra were modeled with an equivalent electrical circuit (inset in Fig. S5) using the Z-View software (Scribner Inc.) [47]. This model allowed us to extract the contributions from the electrolyte (R_{el}), the Li/electrolyte interface, and the Li^+ diffusion resistance (R_d). σ and t^+ were calculated by the following relationships [48,49].

$$\sigma(T) = \frac{l}{S \cdot R_{el}(T)} \tag{3}$$

$$t^+ = \frac{R_{el}}{R_{el} + R_d} \tag{4}$$

Lithium/polymer electrolyte/stainless steel cells were assembled through a single lamination process used to produce the lithium symmetrical cells; they were sealed in airtight pouch bags. The cells were placed inside a climatic chamber at 80 °C and cyclic voltammetry was performed using a VMP3 (Bio-logic) multipotentiostat between −0.5 V up to 6.5 V vs. $Li^+/Li°$ at 1 mV/s.

3. Results and discussion

The PMA*TFSI*-based triblock copolymers were prepared from a PEO(MAMA-SG1)$_2$ macroalkoxyamine which was obtained via the intermolecular radical 1,2-addition of the MAMA-SG1 on a PEO α,ω-diacrylate. This synthetic route is a versatile method to prepare complex macromolecular architectures by NMP. In particular, triblock copolymers such as PS-*b*-PEO-*b*-PS, PS*TFSI*-*b*-PEO-*b*-PS*TFSI*, or PSAN-b-PEO-b-PSAN (PSAN, poly(styrene-co- acrylonitrile)) can be synthesized with this approach [30,50]. A NMP kinetic study of the copolymerization of K-MA*TFSI* and 20 mol% of APEG, compared with K-S*TFSI*, was carried out at 100 °C in water (75 wt%) using PEO(MAMA-SG1)$_2$ as macroinitiator. Kinetic plots of $\ln([M_0]/[M])$ versus $t^{2/3}$ are presented in Fig. 2a where $[M_0]$ and $[M]$ are respectively the initial monomer concentration and the monomer concentration at a given conversion time t. The linearity of these plots proves the well-controlled character of the polymerization [43]. The different PMA*TFSI*-based copolymers were also analysed by SEC. In Fig. 2b, the SEC traces of the reaction mixture sampled at increasing reaction times show unimodal peaks shifting towards lower elution volume (higher M_n). The dispersity of block copolymers, based on PEO calibration, is quite low: between 1.2 and 1.4. These results confirm the well-defined structure of the block copolymers. In addition, a peak at elution volume of 18.2 ml is observed in all samples, including the neat PEO and the mobile phase, and is attributed to the experimental system peak.

Typical DSC curves for the PMA*TFSI* electrolytes are shown in Fig. S6 with w_{BTFSI} values of 0.06, 0.17, 0.27, and 0.43. They are qualitatively similar to those of the PS*TFSI* based electrolytes (data not shown). In Fig. 3a, the melting temperature of the PEO central block ($T_{m,PEO}$) is reported as a function of the weight fraction of TFSI-grafted B blocks (w_{BTFSI}). For comparison, the melting temperature of a neat 35 kg/mol PEO is also shown [20]. For $w_{BTFSI} < 0.3$, $T_{m,PEO}$ is almost independent of the nature and proportion of B*TFSI* blocks with an average value of 54.5 ± 1.5 °C. This value is in agreement with those reported previously for PS*TFSI*-based

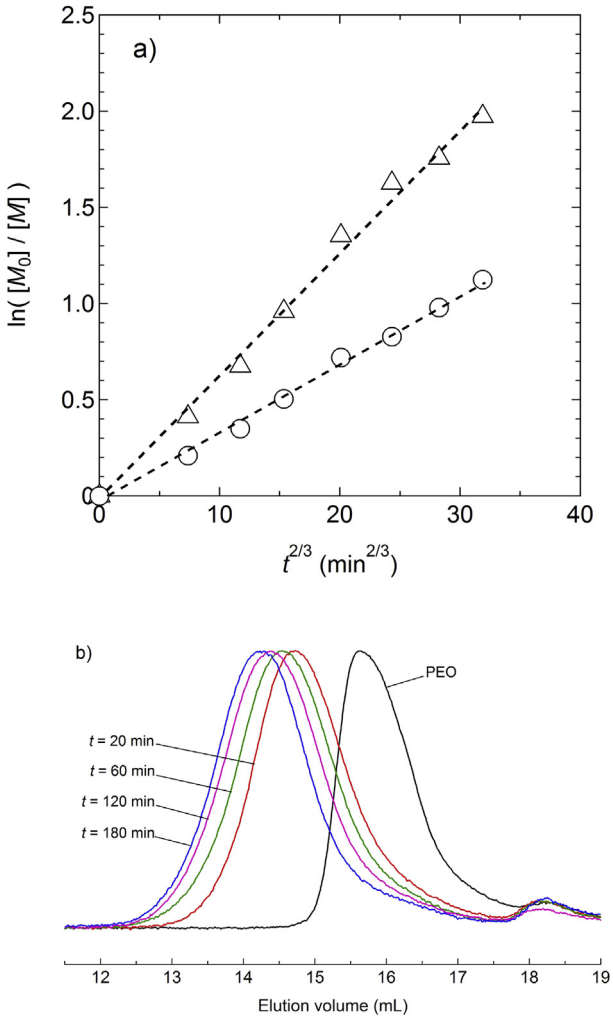

Fig. 2. a) ln([M$_0$]/[M] as a function of $t^{2/3}$ for the copolymerization of K-MA*TFSI* with (△) K-S*TFSI* and (○) K-MA*TFSI* 20%mol of APEGas co-monomer in water (75 wt%) at 100 °C using PEO(MAMA-SG1)$_2$ as macro-initiator. [monomers]/[macroalkox] = 116. b) SEC traces of P(MA*TFSI*-co-APEG)-*b*-PEO-*b*-P(MA*TFSI*-co-APEG) block copolymers at different reaction times. The eluent used was a 50/50 (vol/vol) mixture of an aqueous solution of Na_2HPO_4 (0.15 wt%) and acetonitrile.

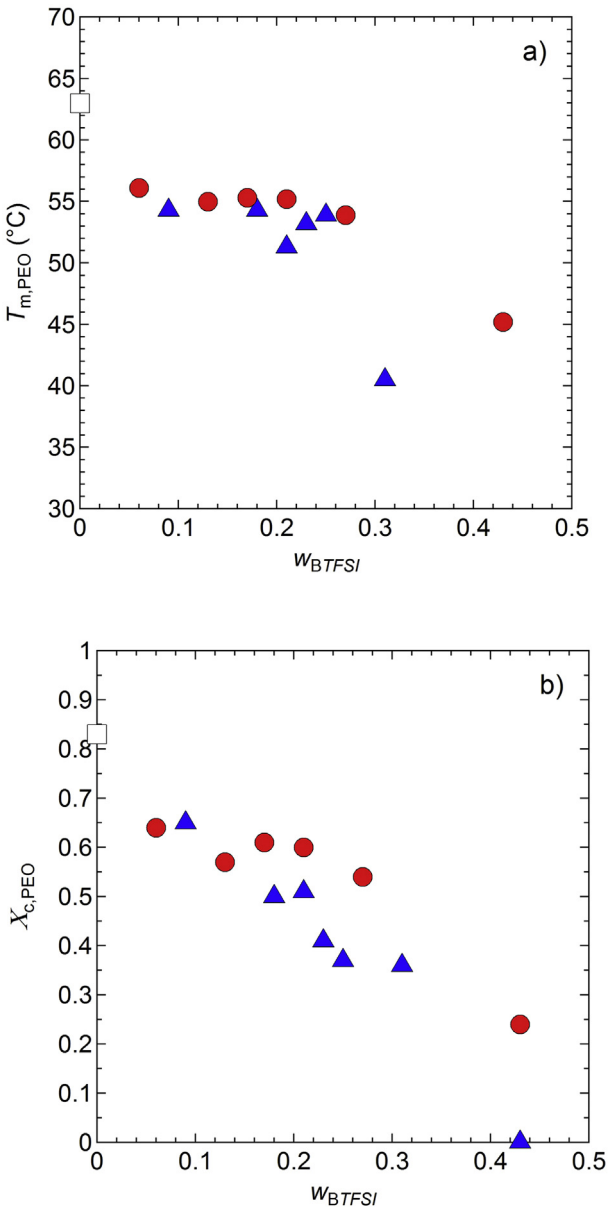

Fig. 3. a) PEO melting temperature, $T_{m,PEO}$, and b) PEO degree of crystallinity, $X_{c,PEO}$, as a function of the weight fraction of B*TFSI* blocks, w_{BTFSI}. The symbols correspond to (▲) PS*TFSI*- and (●) PMA*TFSI*-based electrolytes.

electrolytes [30,51]. For $w_{BTFSI} > 0.3$, $T_{m,PEO}$ decreases sharply down to 40.5 °C for PS*TFSI*_31 and 45.2 °C for PMA*TFSI*_43. We also observe that, among the PMA*TFSI*-based electrolytes, the nature of the co-monomer, a minor component within the electrolyte, has very little influence on the thermodynamic properties. In addition, no evidence of PEO melting peak is observed on the PS*TFSI*_43 DSC curve, as reported previously [30]. This result suggests that a high proportion of B*TFSI* block strongly hinders the PEO crystallization. The PEO degree of crystallinity ($X_{c,PEO}$) is represented as a function of w_{BTFSI} in Fig. 3b. Trends can be distinguished by grouping the data according to the nature of the B*TFSI* block, i.e. PS*TFSI* or PMA*TFSI*. $X_{c,PEO}$ of the PS*TFSI*-based BCEs decreases linearly with w_{BTFSI} from an initial value of 0.83 at $w_{BTFSI} = 0$, corresponding to the neat 35 kg/mol PEO, until $w_{BTFSI} = 0.3$. A similar linear trend was previously reported for PS-PEO-PS block copolymer electrolytes [20]. $X_{c,PEO}$ of the PMA*TFSI* electrolytes also decreases linearly with $w_{PMATFSI}$ until $w_{PMATFSI} = 0.27$, but with a weaker slope. This difference may come from the use of APEG co-monomer in the PMA*TFSI* block, which may act as a compatibilizer agent in the block-copolymer electrolyte, limiting the impact of the "dead zone" at the interface between the blocks [51]. Finally, for all BCEs, $X_{c,PEO}$ drops sharply beyond a threshold value of $w_{BTFSI} \sim 0.3$. The PEO crystallinity is thus strongly linked to the proportion of B*TFSI* block within the single-ion-conductor BCEs. In conclusion, below $w_{BTFSI} = 0.3$, the PEO degree of crystallinity follows a linear trend whereas, beyond $w_{BTFSI} = 0.3$, the PEO domains are mostly amorphous.

The thermal stability of two representative electrolytes, PS*TFSI*_17 and PMA*TFSI*_27, was characterized by TGA under inert atmosphere (Fig. S7). The onset temperature of electrolyte degradation (T_d) of PS*TFSI*_17 is 360 °C, in good agreement with the value of 350 °C reported for PS*TFSI*_31 (with a higher content of PS*TFSI*) [30]. For the PMA*TFSI*_27 electrolyte, two distinct T_d are observed, a first one around 275 °C and then around 345 °C. The weight percentage loss associated to the first degradation event corresponds to about 8%, which is similar to the APEG co-monomer content ($w_C = 0.08$, see Table 1) in this electrolyte. It can therefore be

assumed that the APEG moieties degrade at lower temperature than the other parts of the block copolymer electrolyte.

The microstructure of some representative single-ion-conductor BCEs was studied by SAXS, firstly at room temperature. Fig. 4 represents the SAXS intensity in term of $q^2 \cdot I(q)$ as a function of q (Kratky plot) in order to enhance the scattering peaks. For clarity, the SAXS intensities are shifted by an arbitrary factor. The SAXS patterns of the PS*TFSI*-based electrolytes with w_{PSTFSI} of 0.09, 0.17, 0.23, and 0.28 are shown in Fig. 4a, while those of the PMA*TFSI* with $w_{PMATFSI}$ of 0.06, 0.17, 0.27, and 0.30 are shown in Fig. 4b. All the SAXS diffractograms of the PS*TFSI*-based materials present a first-order peak at almost the same location, $q^* = 0.21 \pm 0.02$ nm^{-1}. The associated domain spacing (d) for each electrolyte, listed in Table 1, is on average 31 ± 3 nm. In addition, some of the diffractograms show a second broad peak located at higher q values, such that the ratio q/q^* is close to but slightly higher than 2. These materials therefore display, at room temperature, a poorly defined lamellar morphology with period almost independent of the composition, i.e. of w_{PSTFSI}, in the range explored here. Balsara and coworkers reported on the microstructure of PEO-PS*TFSI* diblock electrolytes, with a 5 kg/mol PEO [31,32]. A lamellar morphology was also observed but the d spacing increased from 20.4 to 27.8 nm for w_{PSTFSI} increasing from 0.29 to 0.44. This difference may be due to their use of low molecular weight BCEs. The SAXS spectra of the PMA*TFSI*-based electrolytes (Fig. 4b) show similar features as the PS*TFSI*-based electrolytes. The first-order peak positions are independent of the electrolyte composition with an average value of $q^* = 0.22 \pm 0.02$ nm^{-1}. The corresponding d spacing values, on average 30 ± 3 nm (Table 1), are close to those obtained for PS*TFSI*-based electrolytes. For the PMA*TFSI*-based electrolytes, the nature of the co-monomer does not influence the electrolyte microstructure. Thus, at room temperature, the microstructure of all the studied materials is independent of the backbone nature of the functionalized TFSI-grafted block and of the composition, i.e. of the w_{BTFSI} content. To confirm the lamellar morphology, the PMA*TFSI*_17 electrolyte has been characterized by transmission electron microscopy (Fig. S8). A lamellar structure, with alternating bright and dark bands respectively attributed to the PEO and PMA*TFSI* domains, was clearly observed.

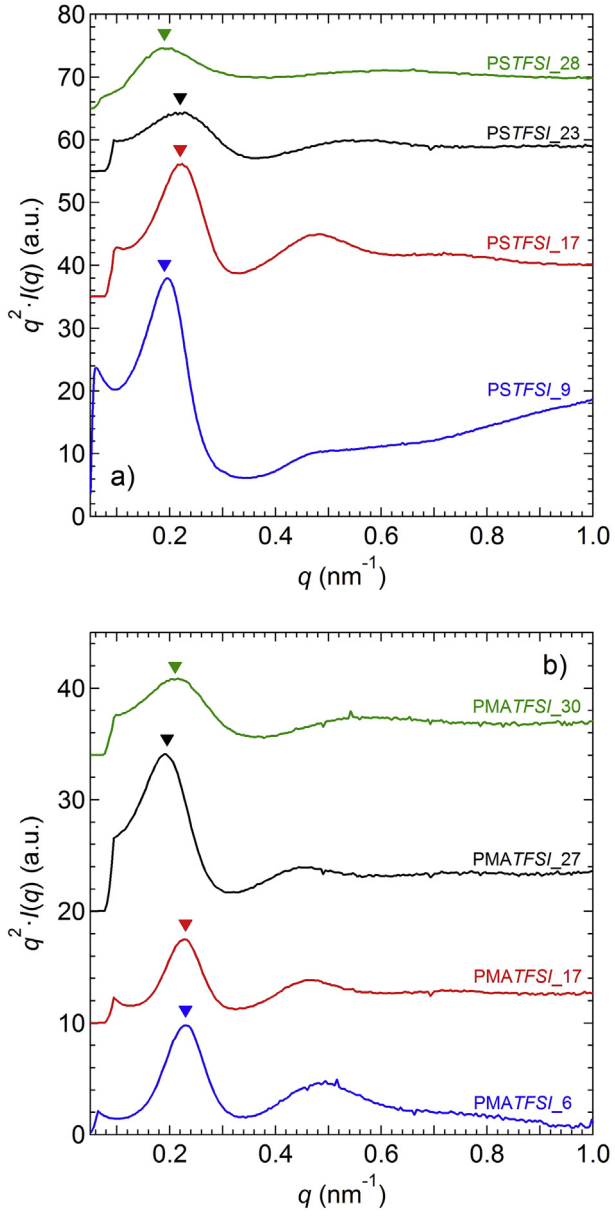

Fig. 4. SAXS intensity, $q^2I(q)$, as a function of the scattering vector modulus, q, at room temperature. a) PS*TFSI*-based electrolytes with w_{PSTFSI} of 0.09, 0.17, 0.23, and 0.28. b) PMA*TFSI*-based electrolytes with $w_{PMATFSI}$ of 0.06, 0.17, and 0.27, and 0.30. The position of the 1st order scattering peak, q^*, is indicated in each curve by an arrowhead.

In a second step, the temperature dependence of the SAXS diffractograms was recorded for two electrolytes, PS*TFSI*_17 and PMA*TFSI*_17, during a heating scan between 35 and 95 °C (Fig. 5). For comparison, the SAXS diffractogram of a neutral PS-PEO-PS triblock copolymer with a central 35 kg/mol PEO block and 0.33 PS weight fraction is also shown. A first- and a second-order peaks are visible on the scattering curves at 35 °C and 50 °C for the PS*TFSI*_17 (Fig. 5a) and PMA*TFSI*_17 (Fig. 5b) electrolytes; they indicate a lamellar morphology. At 65 °C, the disappearance of these peaks is most probably due to an order-to-disorder transition (ODT) occurring between 50 and 65 °C. Based on the study of the thermal properties (Fig. 3), the ODT is clearly related to the melting of the PEO blocks: for $T < T_{m,PEO}$, the morphology is lamellar and for $T > T_{m,PEO}$ the morphology is disordered. This observation about our BCEs agrees very well with the results reported for a diblock PEO-PS*TFSI* as well as those reported for a PMA*TFSI*-PEO-PMA*TFSI* synthesized by RAFT polymerization [31,32,40]. Indeed, for such single-ion-conductor block copolymers, the coincidence of the ODT and the PEO melting temperature suggests that the microstructure results from the PEO crystallization rather than from the incompatibility of the blocks (which is usually the case). The stabilization of the lamellar microstructure by the crystallization of one of the blocks has also been predicted in a theoretical study [52]. In contrast, a scattering peak was observed up to 95 °C for the neat PS-PEO-PS copolymer (Fig. 5c). In this uncharged material, the ODT is not related to the melting of the PEO chains that occurs at 55 °C [20].

For both PS*TFSI*_17 (Fig. 5a) and PMA*TFSI*_17 (Fig. 5b), the position of the first-order scattering peak regularly shifts towards lower q values as the temperature increases. This shift may be due to the gradual melting of PEO crystallites distributed in different sizes. SAXS and WAXS experiments were then performed in between 30 and 67 °C with the PS*TFSI*_28 and PMA*TFSI*_13 electrolytes. Note that the electrolyte compositions are different from those reported in Fig. 5 due to limited available electrolyte amounts. The evolutions with temperature of the lamellar period d and the "degree" of crystallinity of PEO, shown in Fig. 6, were extracted from the position of the first-order reflection in the SAXS diffractograms and the area (A_{PEO}) of the PEO crystalline peak at 19° in the WAXS diffractograms, respectively. In Fig. 6, $T_{m,PEO}$ is indicated by a vertical dotted line corresponding to the average value of

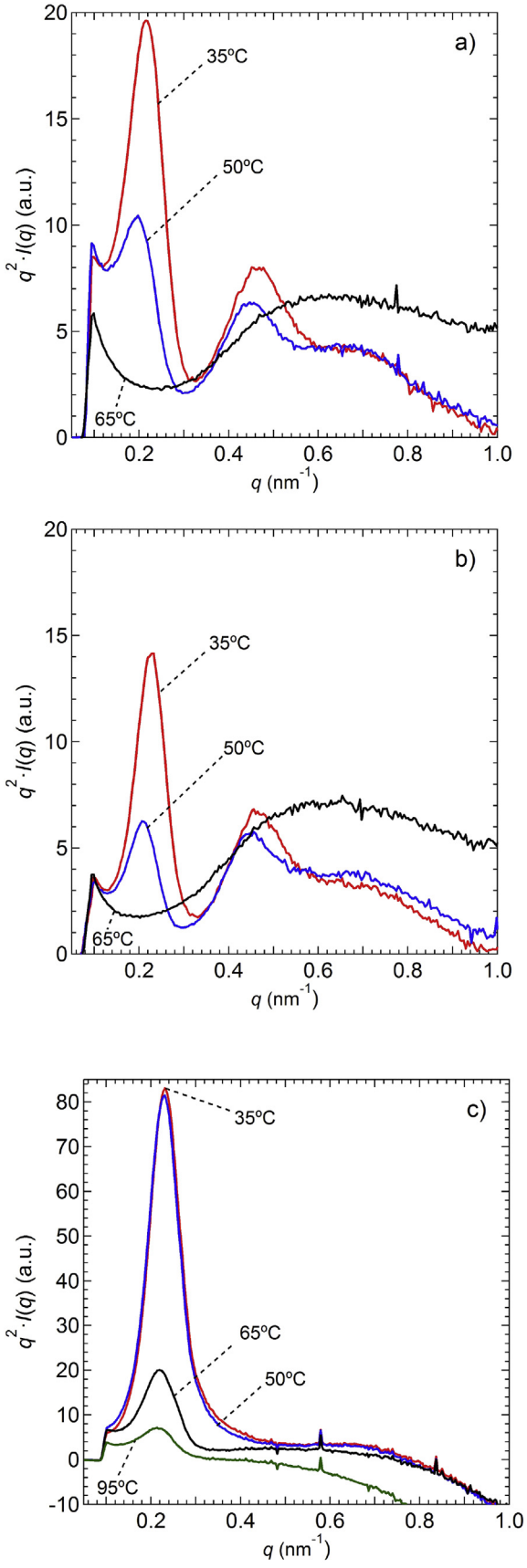

Fig. 5. SAXS intensity, $q^2I(q)$, as a function of the scattering vector modulus, q, between 35 and 95 °C for a) PS*TFSI*_17, b) PMA*TFSI*_17, and c) neat PS-PEO-PS with a central 35 kg/mol PEO block and 0.33 PS weight fraction.

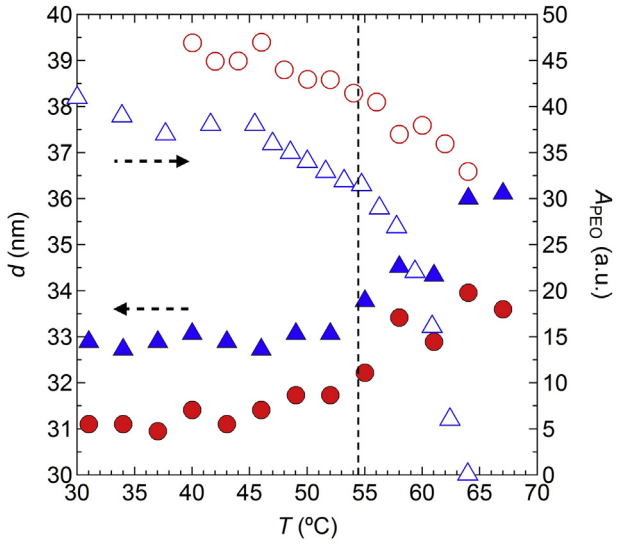

Fig. 6. Temperature dependence of the lamellar period (d, plain symbols) and of the PEO WAXS peak area (A_{PEO}, in arbitrary units, empty symbols) at $\theta = 19°$ for the (▲) PS*TFSI*_28 and (●) PMA*TFSI*_13 electrolytes. The vertical dotted line indicates the average $T_{m,PEO}$ temperature value based on DSC analysis.

54.5 °C ($w_{BTFSI} < 0.3$) based on the DSC analysis (Fig. 3a). For $T < T_{m,PEO}$, d remains constant at about 33 ± 0.1 and 31.3 ± 0.3 nm for the PS*TFSI*_28 and PMA*TFSI*_13 electrolytes, respectively. When the PEO crystallites start to melt at around 45 °C (Fig. S2), d starts to increase smoothly with temperature. The total increase in lamellar period reaches up to ~10% for both materials. In parallel, A_{PEO} decreases with increasing temperature, as the PEO crystallites progressively melt.

The ionic conductivity (σ) of all the electrolytes (Table 1) has been measured between 30 °C and 100 °C. The temperature dependences of σ for the PS*TFSI*-based electrolytes, with w_{PSTFSI} of 0.09, 0.17, 0.23, 0.31, and 0.43, and for the PMA*TFSI*-based electrolytes, with $w_{PMATFSI}$ of 0.06, 0.17, 0.21, 0.30, and 0.43, are shown in Fig. 7a and Fig. 7b, respectively. The conductivity behavior of the PS*TFSI*-based materials is similar to that previously reported in Ref. [30], with a drop at $T_{m,PEO}$, due to the crystallization of the PEO chains, down to very low values, in the range 10^{-8} - 10^{-9} S/cm [20,47]. For $T > T_{m,PEO}$, σ ranges between 1.3×10^{-6} S/cm at 60 °C for PS*TFSI*_43 and 3.3×10^{-5} S/cm at 90 °C for PS*TFSI*_17. In addition, the conductivity of PS*TFSI*_43 does not present any drop in the investigated temperature range, which is consistent with the absence of PEO crystallization as observed by DSC (Fig. 3). In these single-ion-conductor BCEs, the coincidence of the ODT (Fig. 5) with the PEO melting temperature is crucial in ensuring both transfer to and diffusion along the PEO chains of the Li^+ cations.

The evolution of the conductivity of the PMA*TFSI*-based electrolytes (Fig. 7b) is similar to that of the PS*TFSI* materials. For $T > T_{m,PEO}$, σ ranges between 2.7×10^{-6} S/cm at 60 °C for PMA*TFSI*_6 and 6.1×10^{-5} S/cm at 90 °C for PMA*TFSI*_21. Therefore, the ionic conductivities of the electrolytes based on PMA*TFSI* are higher than those based on PS*TFSI* by at least a factor of two.

The electrolyte conductivities at 60 °C are plotted as a function of w_{BTFSI} in Fig. 8. The conductivities of the PS*TFSI* and PMA*TFSI* families show the same trend as both curves display a maximum. For the first family, σ reaches a maximum of 1.1×10^{-5} S/cm for PS*TFSI*_17 whereas, for the second family, σ reaches 2.2×10^{-5} S/cm for PMA*TFSI*_21. The existence of a maximum of the conductivity dependence on salt concentration is classical for concentrated electrolyte systems [10]. The decrease in conductivity at large salt

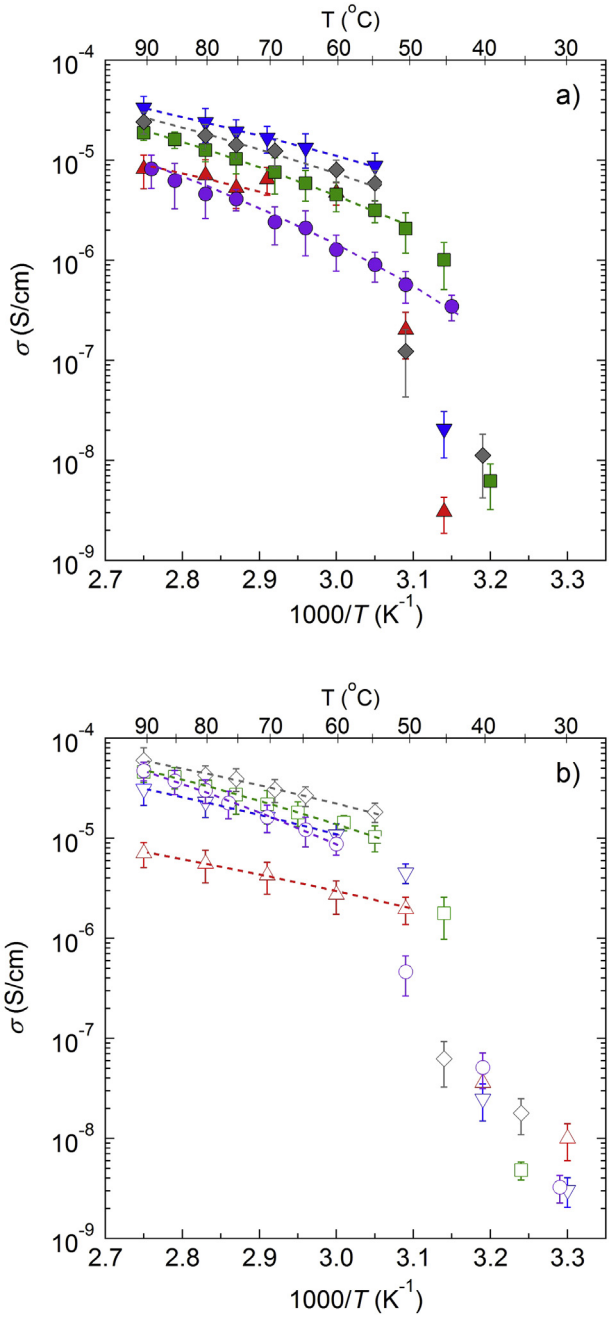

Fig. 7. Ionic conductivity, σ, as a function of the inverse of temperature. a) PS*TFSI*-based electrolytes with w_{PSTFSI} of (▲) 0.09, (▼) 0.17, (◆) 0.23, (■) 0.31 and (●) 0.43. b) PMA*TFSI*- based electrolytes with $w_{PMATFSI}$ of (△) 0.06, (▽) 0.17, (◇) 0.21, (□) 0.30, and (○) 0.43. The dotted lines are the VTF fits using Eq. (5).

content generally arises from both the limited solubility of the salt and a decrease of polymer segmental mobility through Li-ether oxygen association. In addition, we observe that among the PMA*TFSI*-based electrolytes, the nature of the co-monomer, a minor component within the electrolyte structure, has only little influence on the ionic conductivity. Interestingly, for $w_{BTFSI} < 0.17$, σ is independent of the precise nature (PS*TFSI* or PMA*TFSI*) of the B*TFSI* block. However, beyond $w_{BTFSI} = 0.17$, the conductivity of the PS*TFSI*-based electrolytes starts to decrease, whereas that of the PMA*TFSI* electrolytes keeps on increasing till $w_{BTFSI} = 0.21$. Beyond this value, the conductivity of the PMA*TFSI* electrolytes remains

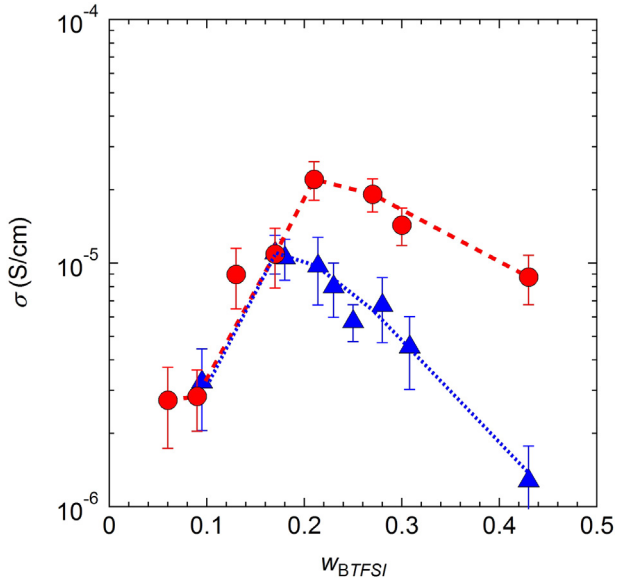

Fig. 8. Isothermal ionic conductivity, σ, at 60 °C as a function of the weight fraction of B*TFSI* block, w_{BTFSI}. The symbols correspond to (▲) PS*TFSI*- and (●) PMA*TFSI*-based electrolytes. The dashed lines are guidelines depending on the nature of the B*TFSI* block.

higher by a factor 2–8 than that of the PS*TFSI* electrolytes. Note that this factor increases with w_{BTFSI}. In terms of electrolyte optimization, grafting the $TFSI^-$ anions onto a methacrylic backbone leads to a better conductivity compared to a polystyrene backbone. Thus, tuning the backbone nature of the *TFSI*-grafted block is an important step to optimize the ionic conductivity of single-ion conductor BCEs.

To investigate the cationic transport properties, the Li transference number (t^+) was determined by AC impedance spectroscopy at 90 °C for all the electrolytes listed in Table 1. t^+ is reported as a function of w_{BTFSI} in Fig. 9. For comparison, a high molecular weight PEO/LiTFSI (EO/Li = 30) data point was also included [53]. The Li transference number of the PEO homopolymer electrolyte is approximately 0.15 whereas those of all the B*TFSI*-based electrolytes are close to 1, independently of the electrolyte composition. More precisely, the PS*TFSI*-based electrolytes have a t^+ of 0.88 ± 0.03, which is similar to that already reported [30], whereas t^+ of the PMA*TFSI*-based electrolytes is 0.84 ± 0.03, a value close to that obtained by Mecerreyes and coworkers [40]. In practice, transference numbers measured in single-ion-conductor polymers usually lie between 0.85 and 0.95 (see for example Refs [30, 40, 54]). In principle, the transference number of our BCEs is structurally equal to 1 because the anions are grafted on the polymer backbones and therefore cannot move over long distances. In our case, we observe a small diffusion loop in the impedance spectra (see Fig. S5). Of course, we cannot exclude the existence of a very small amount of unreacted anionic monomers, although ^{1}H NMR spectra of the final products did not show the presence of any anionic monomers (see in Supplementary Materials Figs. S1–S4). Reducing t^+ from 1 to 0.88 (PS*TFSI*) or 0.84 (PMA*TFSI*) would require a high level of ionic impurities, on the order of 10–20 mM, which seems quite unlikely in our polymers. On the other hand, passive layers appear at the surface of the Li electrode, due to its high reactivity. These passive layers are composed mainly of Li oxides and compounds produced by the reaction of the polymer electrolyte with the Li surface. All these passive layers are generally very thin (from a few nm to tens of nm thick) and are globally described in literature as “Solid Electrolyte Interphases”, with a $t^+ = 1$ [55].

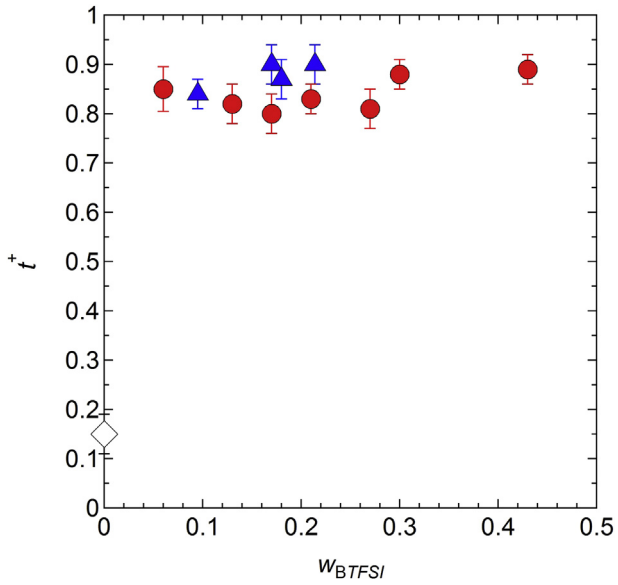

Fig. 9. Lithium transference number (t^+) versus the weight fraction of B*TFSI* blocks, w_{BTFSI}, at 90 °C. The symbols correspond to (▲) PS*TFSI*- and (●) PMA*TFSI*-based electrolytes. For comparison, the data (◇) of a PEO/LiTFSI (EO/Li = 30) electrolyte is included [52].

However, these passive layers may not behave as pure single-ion-conductors, with a low electronic conductivity for the inorganic part. Moreover, the grafted anions of the polymeric compounds of the passive layers can still retain some local mobility and still play a role in transport over such a small thickness. The low-frequency diffusion loop observed by impedance spectroscopy (Fig. S1) can then be due to ionic diffusion through the passive layers present on the Li surface [30]. We thus confirm, as expected, the single-ion-conductor behavior for all the BCEs investigated in this work.

In order to probe the ionic transport mechanism of the single-ion conductor BCEs, the conductivity has been fitted with the empirical Vogel-Tamman-Fulcher (VTF) equation [56–58]:

$$\sigma = \frac{A}{\sqrt{T}} \cdot exp\left(\frac{-B}{R \cdot (T - T_0)}\right) \quad (5)$$

where the three free parameters are the pre-exponential factor, A, linked to the amount of free charges and to the time constant related to the ion dynamics, the pseudo activation energy, B, linked to the critical free volume needed for the ions to move, and the ideal glass transition temperature, T_0, where the available free volume is null, and which is generally estimated by $T_g - 50$ K [59].

We assume that the ionic transport mechanism in the single-ion-conductor BCEs is similar to that in high molecular weight PEO/LiTFSI where the Li^+ ions move in the PEO matrix via a hopping mechanism governed by the redistribution of the free volume excess [53]. Consequently, we consider that the pseudo activation energy, B, of the VTF equation is the same for all electrolytes and equal to that of high molecular weight PEO/LiTFSI, i.e. 7.8 kJ/mol [53]. The remaining two free parameters in Eq. (5), A and T_0, were then adjusted to fit the conductivity data for $T > T_{m,PEO}$. These two parameters, taken from the best fits ($\chi^2 > 0.99$) of the PS*TFSI* and PMA*TFSI* series are presented in Fig. 10 as a function of w_{BTFSI}. The A parameter (Fig. 10a) of the PMA*TFSI*-based electrolytes increases linearly with $w_{PMATFSI}$ between 0.02 and 0.59 $S.K^{0.5}$/cm. For the PS*TFSI*-based electrolytes, A first increases with w_{PSTFSI}, taking values similar to that of the PMA*TFSI*-based electrolytes, then A levels off at 0.17 ± 0.02 $S.K^{0.5}$/cm for $w_{BTFSI} \geq 0.17$. The T_0 parameter

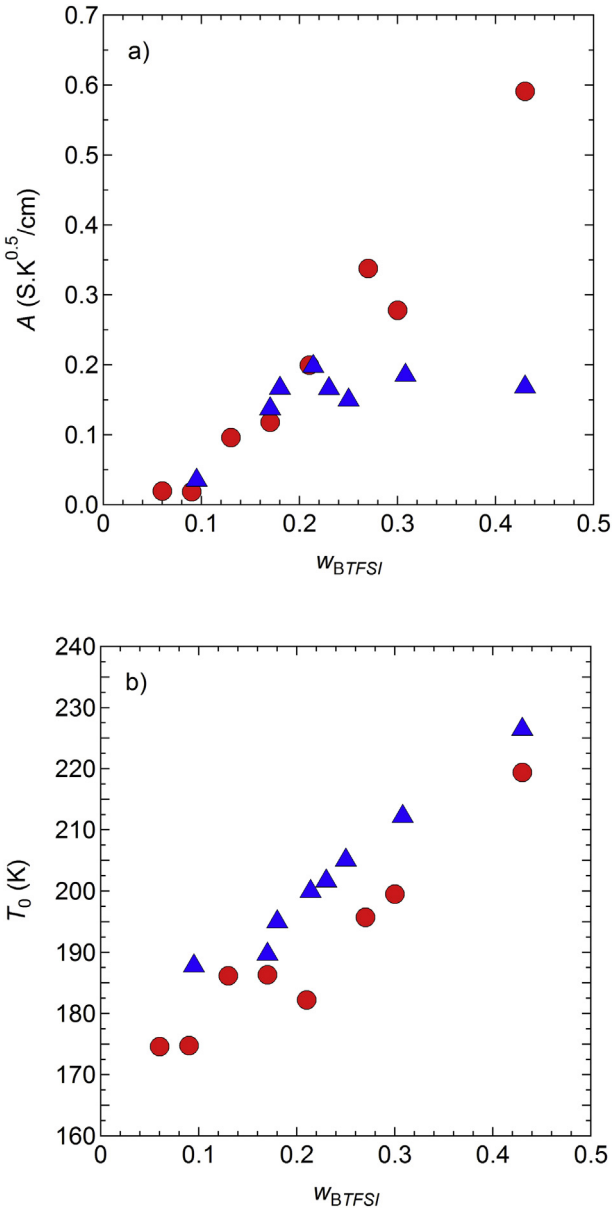

Fig. 10. Evolution of the parameters a) A and b) T_0 of the VTF equation as a function of w_{BTFSI}. The symbols correspond to (▲) PS*TFSI*- and (●) PMA*TFSI*-based electrolytes. The VTF parameter B is taken constant and equal to 7.8 kJ/mol.

(Fig. 10b), for both PS*TFSI*- and PMA*TFSI*-based electrolytes, increases linearly with w_{BTFSI} from 175 to 226 K. The values for the PS*TFSI* series are slightly higher than those of the PMA*TFSI* series. Interestingly, the intercept at $w_{BTFSI} = 0$ for both series gives a T_0 value of 168 ± 2 K, which corresponds to the T_g of a high molecular weight PEO/LiTFSI electrolyte − 50 K. [10,53], Thus, for the PS*TFSI*-based electrolytes, the amount of free charges seems to remain constant above w_{PSTFSI} of 0.17 while the polymer dynamics ($T_g = T_0 + 50$ K) slows down as w_{PSTFSI} increases. The combination of these two effects explains the dependence of the ionic conductivity on w_{PSTFSI}, with the presence of a maximum at $w_{PSTFSI} = 0.17$ (Fig. 8).

To further understand the limiting factor that controls the ionic transport, the influence of the Li concentration (C_{Li}), in mol per kg of electrolyte, on the glass transition temperature, $T_g = T_0 + 50$ K, was investigated (Fig. S9) for both PS*TFSI*- and PMA*TFSI*-based electrolytes and compared with that of the reference PEO/LiTFSI

electrolyte [10]. In contrast with the behavior of the latter, the T_g of the single-ion conductor BCEs increases linearly with C_{Li} and takes values higher by about 25 °C. This demonstrates the strong effect of the polymer dynamics on the ionic transport in PS*TFSI*- and PMA*TFSI*-based electrolytes. Therefore, compared to PEO/LiTFSI, the lower conductivity, at a given temperature, of the single-ion-conductor BCEs could be due to their higher glass transition temperature. In addition, it is interesting to note that the values of T_g obtained here by VTF fits ($T_g = T_0 + 50$ K) are in very good agreement with the values predicted by the Fox law ($T_{g,Fox}$) [60], given in Eq. (6), for the single-ion conductor BCEs reported here (see Table 1).

$$\frac{1}{T_{g,Fox}} = \frac{w_{EO}}{T_{g,PEO}} + \frac{w_{BTFSI}}{T_{g,BTFSI}} + \frac{w_C}{T_{g,c}} \quad (6)$$

with $T_{g,PEO}$ (−55 °C) [10], $T_{g,BTFSI}$ (152 and 95 °C for PS*TFSI* and PMA*TFSI*, respectively) [40,41], and $T_{g,c}$ (−70 °C for the APEG polymer and 152 °C for PS*TFSI*) [41,61] the glass transition temperature of the PEO, B*TFSI*, and co-monomers, respectively. The relative discrepancy between the values of T_0 derived from Eq. (6) ($T_{0,Fox} = T_{g,Fox} - 50$ K) and from the VTF fits of the ionic conductivity (Eq. (5)) is lower than 3% (Fig. S10), which confirms that the two B*TFSI* and PEO blocks are fairly miscible above the melting temperature of PEO. Furthermore, this means that the ionic motion in these single-ion-conductor BCEs is essentially determined by the electrolyte glass transition temperature.

We now discuss the reduced ionic conductivity (σ_r), which is the ionic conductivity at a temperature such that the difference T - T_g is kept constant [10], to 110 °C in this case. σ_r only reflects the effect of the concentration of free Li^+ ions within the electrolytes on the ionic transport because the polymer dynamics is the same for each set of electrolytes. To fully compare the behavior of the single-ion conductor BCEs with that of PEO/LiTFSI electrolytes [10], the product of the transference number (t^+) with σ_r is plotted as a function of C_{Li} in Fig. 11 t^+ is taken as unity for the single-ion-conductor BCEs, whereas it is $t^+ = 0.15$ for the PEO/LiTFSI electrolytes [53]. For the PEO/LiTFSI electrolytes, $t^+ \times \sigma_r$ increases almost linearly with C_{Li} up to 1.8 mol/kg and then drops sharply.

For the PMA*TFSI*-based electrolytes, $t^+ \times \sigma_r$ also increases linearly with C_{Li} with a similar slope as that of PEO/LiTFSI, up to the highest investigated value of C_{Li} (1.24 mol/kg). On average, $t^+ \times \sigma_r$ of the PMA*TFSI* series is lower than that of the PEO/LiTFSI electrolytes by 2.3×10^{-5} S/cm. This may come from a too heterogeneous distribution of the ion-bearing structural blocks in the PEO matrix, which prevents the B*TFSI* domains from percolating throughout the whole sample. The main factor that controls the overall ionic motion mechanism of the PMA*TFSI*-based electrolytes is the evolution of the T_g rather than a limitation in the amount of available free charges.

For the PS*TFSI*-based electrolytes, $t^+ \times \sigma_r$ also increases linearly with C_{Li} up to 0.53 mol/kg, taking similar values as the PMA*TFSI* series, and then it levels off. This confirms that the ion dynamics in PS*TFSI*-based electrolytes is actually limited by the amount of available free charges. The amount of free Li^+ ions within the PMA*TFSI*-based electrolytes is thus higher than that of the PS*TFSI*-based electrolytes at high concentration ($C_{Li} > 0.53$ mol/kg). This leads to a conductivity maximum occurring at higher content of B*TFSI* block for the former electrolytes (Fig. 8). This effect is probably due to a better compatibility of the PEO blocks with the PMA*TFSI* blocks, compared to the PS*TFSI* blocks, which allows for a higher solubility of Li*TFSI* in the conducting PEO domains.

According to our approach, for single-ion conductor PEO-based electrolytes, the Li^+ ionic conductivity in molten PEO/LiTFSI electrolyte would represent an upper theoretical conductivity limit. Therefore, optimization of single-ion-conductor BCEs lies mostly in the improvement of the block compatibility. This can be achieved by a careful choice of the nature of the backbone of the B*TFSI* block and by enhancing the B*TFSI* block segmental dynamics (T_g), to improve ionic transport.

For battery applications, the electrochemical stability window is an essential parameter as it defines the potential interval where the electrolyte remains stable towards the electrochemical reactions

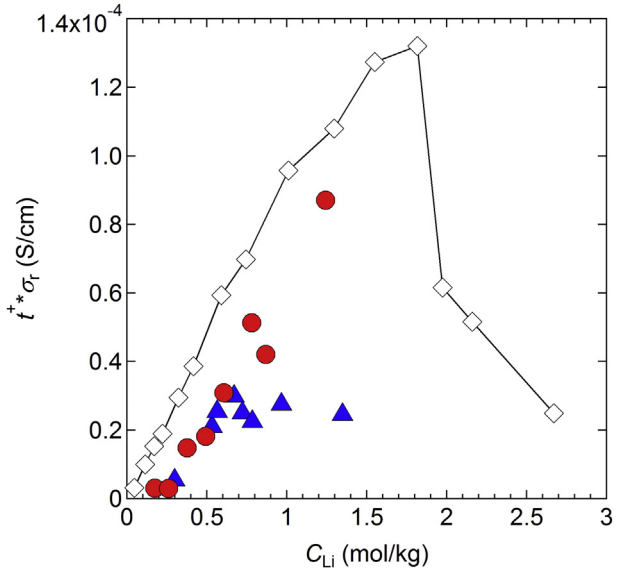

Fig. 11. Product of the Li^+ transference number, t^+, with the reduced ionic conductivity, σ_r, at $T - T_g = 110$ °C as a function of the Li concentration, C_{Li}, in mol per kg of electrolyte. The symbols correspond to (▲) PS*TFSI*- and (●) PMA*TFSI*-based electrolytes. For comparison, the data (◇) of a PEO/LiTFSI, considering a t^+ of 0.15, is also shown [10,52].

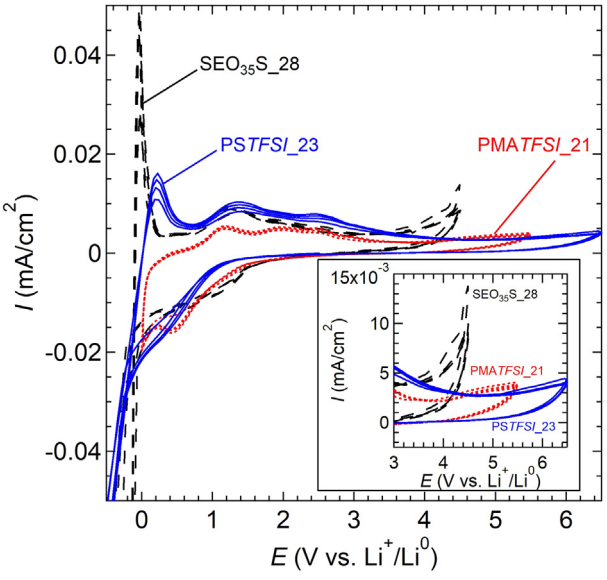

Fig. 12. Cyclic voltammograms recorded at 1 mV/s and 80 °C between −0.5 and 6.5 V vs Li^+/Li^0 for four consecutive cycles, using PS*TFSI*_23 (solid blue curve), PMA*TFSI*_21 (dotted red curve), and neutral $SEO_{35}S$_28 (dashed black curve) triblock copolymer electrolytes. The inset is a zoom in between 3 and 6.5 V vs Li^+/Li^0. (For interpretation of the references to colour in this figure legend, the reader is referred to the Web version of this article.)

taking place at the battery electrodes. Cyclic voltammetry was performed on two representative electrolytes: PS*TFSI*_28 and PMA*TFSI*_21, at 80 °C. Fig. 12 represents the current density (I) as a function of the potential (E) versus Li^+/Li^0 for four consecutive cycles recorded at 1 mV/s between −0.5 and 6.5 V vs. Li^+/Li^0. For comparison, a PS-PEO-PS copolymer, with a central 35 kg/mol PEO block and 0.28 PS weight fraction, doped with LiTFSI at EO:Li = 25, labeled $SEO_{35}S\_28$, is also reported [20]. In agreement with literature data, the electrolytes present a low-potential wall ascribed to the Li^+/Li^0 couple [62]. The electrochemical stability window of the neutral BCE is equivalent to that of the PEO homopolymer electrolyte, i.e. up to 3.8 V vs. Li^+/Li^0 [20,63]. The PSTFSI_28 electrolyte has a stability window extended up to 4.5 V vs. Li^+/Li^0 whereas, in contrast, the PMATFSI_21 stability window is limited to about 4 V vs. Li^+/Li^0 (see inset of Fig. 12). This result can be explained by the better compatibility between PEO and PMA*TFSI* blocks, compared to PS*TFSI* blocks, leading to a stainless steel/electrolyte interface in which PEO is the predominant domain. Therefore, the electrochemical stability window of the PMA*TFSI* electrolytes is close to that of the PEO homopolymer electrolyte.

4. Conclusion

Two families of single-ion conductor BCEs with PEO as conducting block and either PS*TFSI* or PMA*TFSI* as structural block have been synthesized and characterized. Above a weight fraction of B*TFSI* block, $w_{BTFSI} = 0.3$, the thermodynamic properties of the PEO block (melting temperature and degree of crystallinity) are strongly altered. X-ray scattering experiments have revealed that, at temperatures below the PEO melting temperature, the microstructure of the single-ion conductor electrolytes displays a poorly defined lamellar morphology, with period almost independent of the composition. Moreover, the order-to-disorder transition coincides with the PEO melting temperature, which shows that the morphology is governed by the crystallinity of the PEO block. Although the ionic conductivity of the PS*TFSI*-based electrolytes is already among the best reported so far for dry single-ion-conductor solid polymer electrolytes, the conductivity of the PMA*TFSI*-based electrolytes is even larger, at high salt concentration, by at least a factor of two. All the block copolymer electrolytes reported here behave as single-ion conductors, independently of the nature of the structural block. For the PS*TFSI*-based electrolytes, we interpret the existence of a conductivity maximum at $w_{PSTFSI} = 0.17$ by a limitation in available free charges at high salt concentration while the polymer dynamics slows down as w_{PSTFSI} increases. Finally, because we use a PEO matrix, we cannot a priori expect, for a single-ion-conductor, a conductivity better than that of PEO multiplied by the transference number. Taking $t^+ = 0.15$, this would correspond to 7.5×10^{-5} S/cm at 60 °C. For the PMA*TFSI* systems, we have obtained a value of 2.2×10^{-5} S/cm. This value lower by a factor of 3.5 can be mostly interpreted, according to our detailed study of the reduced ionic conductivity, by the increase of glass transition temperature in these BCEs compared to PEO. Thus, we believe that to reach a higher conductivity, while keeping a PEO matrix, we should select an anionic block with T_g as low as possible. Moreover, choosing anions with a better delocalisation of the negative charge [39] and a higher local dynamics (inserting a spacer between the polymer backbone and the anion, for example) would help Lithium ion dissociation and solvation by the PEO matrix.

Acknowledgments

The present work was undertaken within the French ANR program PROGELEC under the contract COPOLIBAT2, no. ANR-13-PRGE-0002-01.

Appendix A. Supplementary data

Supplementary data related to this article can be found at https://doi.org/10.1016/j.electacta.2018.02.142.

References

[1] H. Ibrahim, A. Ilinca, J. Perron, Energy storage systems-characteristics and comparisons, Renew. Sustain. Energy Rev. 12 (2008) 1221–1250.
[2] M. Armand, J.-M. Tarascon, Building better batteries, Nature 451 (2008) 652–657.
[3] Z. Yang, J. Zhang, M.C.W. Kintner-Meyer, X. Lu, D. Choi, J.P. Lemmon, J. Liu, Electrochemical energy storage for green grid, Chem. Rev. 111 (2011) 3577–3613.
[4] K. Xu, Nonaqueous liquid electrolytes for lithium-based rechargeable batteries, Chem. Rev. 104 (2004) 4303–4417.
[5] A. Hammami, N. Raymond, M. Armand, Runaway risk of forming toxic compounds, Nature 424 (2003) 635–636.
[6] J.-M. Tarascon, M. Armand, Issues and challenges facing rechargeable lithium batteries, Nature 414 (2001) 359–367.
[7] M. Armand, The history of polymer electrolytes, Solid State Ionics 69 (1994) 309–319.
[8] D. Baril, C. Michot, M. Armand, Electrochemistry of liquids vs. solids: polymer electrolytes, Solid State Ionics 94 (1997) 35–47.
[9] J. Shi, C.A. Vincent, The effect of molecular-weight on cation mobility in polymer electrolytes, Solid State Ionics 60 (1993) 11–17.
[10] S. Lascaud, M. Perrier, A. Vallée, S. Besner, J. Prudhomme, M. Armand, Phase-diagrams and conductivity behavior of poly(ethylene oxide) molten-salt rubbery electrolytes, Macromolecules 27 (1994) 7469–7477.
[11] M. Dollé, L. Sannier, B. Beaudoin, M. Trentin, J.-M. Tarascon, Live scanning electron microscope observations of dendritic growth in lithium/polymer cells, Electrochem. Solid State Lett. 5 (2002) A286–A289.
[12] M. Rosso, C. Brissot, A. Teyssot, M. Dollé, L. Sannier, J.-M. Tarascon, R. Bouchet, S. Lascaud, Dendrite short-circuit and fuse effect on Li/polymer/Li cells, Electrochim. Acta 51 (2006) 5334–5340.
[13] D.R. Sadoway, Block and graft copolymer, electrolytes for high-performance, solid-state, lithium batteries, J. Power Sources 129 (2004) 1–3.
[14] T. Niitani, M. Shimada, K. Kawamura, K. Kanamura, Characteristics of new-type solid polymer electrolyte controlling nano-structure, J. Power Sources 146 (2005) 386–390.
[15] M. Singh, O. Odusanya, G.M. Wilmes, H.B. Eitouni, E.D. Gomez, A.J. Patel, V.L. Chen, M.J. Park, P. Fragouli, H. Iatrou, N. Hadjichristidis, D. Cookson, N.P. Balsara, Effect of molecular weight on the mechanical and electrical properties of block copolymer electrolytes, Macromolecules 40 (2007) 4578–4585.
[16] R. Bouchet, T.N.T. Phan, E. Beaudoin, D. Devaux, P. Davidson, D. Bertin, R. Denoyel, Charge transport in nanostructured PS-PEO-PS triblock copolymer electrolytes, Macromolecules 47 (2014) 2659–2665.
[17] V. Abetz, T. Goldacker, Formation of superlattices via blending of block copolymers, Macromol. Rapid Commun. 21 (2000) 16–34.
[18] M.W. Matsen, R.B. Thompson, Equilibrium behavior of symmetric ABA triblock copolymer melts, J. Chem. Phys. 111 (1999) 7139–7146.
[19] A. Panday, S. Mullin, E.D. Gomez, N. Wanakule, V.L. Chen, A. Hexemer, J. Pople, N.P. Balsara, Effect of molecular weight and salt concentration on conductivity of block copolymer electrolytes, Macromolecules 42 (2009) 4632–4637.
[20] D. Devaux, D. Glé, T.N.T. Phan, D. Gigmes, E. Giroud, M. Deschamps, R. Denoyel, R. Bouchet, Optimization of block copolymer electrolytes for lithium metal batteries, Chem. Mater. 27 (2015) 4682–4692.
[21] P. Lobitz, H. Fullbier, A. Reiche, J.C. Illner, H. Reuter, S. Horing, Ionic-conductivity in poly(Ethylene Oxide) poly(alkylmethacrylate) block copolymer mixtures with LiI, Solid State Ionics 58 (1992) 41–48.
[22] P.P. Soo, B.Y. Huang, Y.I. Jang, Y.M. Chiang, D.R. Sadoway, A.M. Mayes, Rubbery block copolymer electrolytes for solid-state rechargeable lithium batteries, J. Electrochem. Soc. 146 (1999) 32–37.
[23] T. Niitani, M. Amaike, H. Nakano, K. Dokko, K. Kanamura, Star-shaped polymer electrolyte with microphase separation structure for all-solid-state lithium batteries, J. Electrochem. Soc. 156 (2009) A577–A583.
[24] K.J. Harry, D.T. Hallinan, D.Y. Parkinson, A.A. MacDowell, N.P. Balsara, Detection of subsurface structures underneath dendrites formed on cycled lithium metal electrodes, Nat. Mater. 13 (2014) 69–73.
[25] N.S. Schauser, K.J. Harry, D.Y. Parkinson, H. Watanabe, N.P. Balsara, Lithium dendrite growth in glassy and rubbery nanostructured block copolymer electrolytes, J. Electrochem. Soc. 162 (2015) A398–A405.
[26] D. Devaux, X. Wang, J.L. Thelen, D.Y. Parkinson, J. Cabana, F. Wang, N.P. Balsara, Lithium metal-copper vanadium oxide battery with a block copolymer electrolyte, J. Electrochem. Soc. 163 (2016) A2447–A2455.
[27] M. Doyle, T.F. Fuller, J. Newman, The importance of the lithium ion transference number in lithium/polymer cells, Electrochim. Acta 39 (1994) 2073–2081.
[28] J.-N. Chazalviel, Electrochemical aspects of the generation of ramified metallic electrodeposits, Phys. Rev. A 42 (1990) 7355–7367.
[29] S.W. Ryu, P.E. Trapa, S.C. Olugebefola, J.A. Gonzalez-Leon, D.R. Sadoway, A.M. Mayes, Effect of counter ion placement on conductivity in single-ion

conducting block copolymer electrolytes, J. Electrochem. Soc. 152 (2005) A158–A163.
[30] R. Bouchet, S. Maria, R. Meziane, A. Aboulaich, L. Lienafa, J.-P. Bonnet, T.N.T. Phan, D. Bertin, D. Gigmes, D. Devaux, R. Denoyel, M. Armand, Single-ion BAB triblock copolymers as highly efficient electrolytes for lithium-metal batteries, Nat. Mater. 12 (2013) 452.
[31] S. Inceoglu, A. Rojas, D. Devaux, X.C. Chen, G.M. Stone, N.P. Balsara, Morphology-conductivity relationship in single-ion-conducting block copolymer electrolytes for lithium batteries, ACS Macro Lett. 3 (2014) 510–514.
[32] A.A. Rojas, S. Inceoglu, N.G. Mackay, J.L. Thelen, D. Devaux, G. Stone, N.P. Balsara, Effect of lithium-ion concentration on morphology and ion transport in single-ion-conducting block copolymer electrolytes, Macromolecules 48 (2015) 6589–6595.
[33] Y. Zhang, C.A. Lim, W. Cai, R. Rohan, G. Xu, Y. Sun, H. Cheng, Design and synthesis of a single ion conducting block copolymer electrolyte with multi-functionality for lithium ion batteries, RSC Adv. 4 (2014) 43857–43864.
[34] C. Jangu, A.M. Savage, Z. Zhang, A.R. Schultz, L.A. Madsen, F.L. Beyer, T.E. Long, Sulfonimide-containing triblock copolymers for improved conductivity and mechanical performance, Macromolecules 48 (2015) 4520–4528.
[35] L. Porcarelli, A.S. Shaplov, F. Bella, J.R. Nair, D. Mecerreyes, C. Gerbaldi, Single-ion conducting polymer electrolytes for lithium metal polymer batteries that operate at ambient temperature, ACS Energy Lett. 1 (2016) 678–682.
[36] Y. Chen, H. Ke, D. Zeng, Y. Zhang, Y. Sun, H. Cheng, Superior polymer backbone with poly(arylene ether) over polyamide for single ion conducting polymer electrolytes, J. Membr. Sci. 525 (2017) 349–358.
[37] L. Porcarelli, K. Manojkumar, H. Sardon, O. Llorente, A.S. Shaplov, K. Vijayakrishna, C. Gerbaldi, D. Mecerreyes, Single ion conducting polymer electrolytes based on versatile polyurethanes, Electrochim. Acta 241 (2017) 526–534.
[38] L. Porcarelli, A.S. Shaplov, M. Salsamendi, J.R. Nair, Y.S. Vygodskii, D. Mecerreyes, C. Gerbaldi, Single-ion block copoly(ionic liquid)s as electrolytes for all-solid state lithium batteries, ACS Appl. Mater. Interfaces 8 (2016) 10350–10359.
[39] Q. Ma, H. Zhang, C. Zhou, L. Zheng, P. Cheng, J. Nie, W. Feng, Y.-S. Hu, H. Li, X. Huang, L. Chen, M. Armand, Z. Zhou, Single lithium-ion conducting polymer electrolytes based on a super-delocalized polyanion, Angew. Chem. Int. Ed. 55 (2016) 2521–2525.
[40] L. Porcarelli, M.A. Aboudzadeh, L. Rubatat, J.R. Nair, A.S. Shaplov, C. Gerbaldi, D. Mecerreyes, Single-ion triblock copolymer electrolytes based on poly(-ethylene oxide) and methacrylic sulfonamide blocks for lithium metal batteries, J. Power Sources 364 (2017) 191–199.
[41] R. Meziane, J.-P. Bonnet, M. Courty, K. Djellab, M. Armand, Single-ion polymer electrolytes based on a delocalized polyanion for lithium batteries, Electrochim. Acta 57 (2011) 14–19.
[42] A.S. Shaplov, P.S. Vlasov, M. Armand, E.I. Lozinskaya, D.O. Ponkratov, I.A. Malyshkina, F. Vidal, O.V. Okatova, G.M. Pavlov, C. Wandrey, I.A. Godovikov, Y.S. Vygodskii, Design and synthesis of new anionic "polymeric ionic liquids" with high charge delocalization, Polym. Chem. 2 (2011) 2609–2618.
[43] T.N.T. Phan, A. Ferrand, H.T. Ho, L. Lienafa, M. Rollet, S. Maria, R. Bouchet, D. Gigmes, Vinyl monomers bearing a sulfonyl(trifluoromethane sulfonyl) imide group: synthesis and polymerization using nitroxide-mediated polymerization, Polym. Chem. 7 (2016) 6901–6910.
[44] M. Marzantowicz, F. Krok, J.R. Dygas, Z. Florjanczyk, E. Zygadlo-Monikowska, The influence of phase segregation on properties of semicrystalline PEO: LiTFSI electrolytes, Solid State Ionics 179 (2008) 1670–1678.
[45] L.O. Griffin, Physical Constants of Linear Homopolymers, Springer Verlag, Berlin, 1968.
[46] M. Impéror-Clerc, P. Davidson, An X-ray scattering study of flow-aligned samples of a lyotropic liquid-crystalline hexagonal phase, Eur. Phys. J. B. 9 (1999) 93–104.
[47] R. Bouchet, S. Lascaud, M. Rosso, An EIS study of the anode Li/PEO-LiTFSI of a Li polymer battery, J. Electrochem. Soc. 150 (2003) A1385–A1389.
[48] P.R. Sørensen, T. Jacobsen, Conductivity, charge-transfer and transport number - an AC-investigation of the polymer electrolyte LiSCN-Poly(Ethyleneoxide), Electrochim. Acta 27 (1982) 1671–1675.
[49] J. Ross MacDonald, Impedance/admittance response of a binary electrolyte, Electrochim. Acta 37 (1992) 1007–1014.
[50] D. Quémener, G. Bonniol, T.N.T. Phan, D. Gigmes, D. Bertin, A. Deratani, Free-standing nanomaterials from block copolymer self-assembly, Macromolecules 43 (2010) 5060–5065.
[51] E. Beaudoin, T.N.T. Phan, M. Robinet, R. Denoyel, P. Davidson, D. Bertin, R. Bouchet, Effect of interfaces on the melting of PEO confined in triblock PS-b-PEO-b-PS copolymers, Langmuir 29 (2013) 10874–10880.
[52] E.A. DiMarzio, C.M. Guttman, J.D. Hoffman, Calculation of lamellar thickness in a diblock copolymer, one of whose components is crystalline, Macromolecules 13 (1980) 1194–1198.
[53] D. Devaux, R. Bouchet, D. Glé, R. Denoyel, Mechanism of ion transport in PEO/LiTFSI complexes: effect of temperature, molecular weight and end groups, Solid State Ionics 227 (2012) 119–127.
[54] Y. Zhang, W. Cai, R. Rohan, M. Pan, Y. Liu, X. Liu, C. Li, Y. Sun, H. Cheng, Toward ambient temperature operation with all-solid-state lithium metal batteries with a sp3 boron-based solid single ion conducting polymer electrolyte, J. Power Sources 306 (2016) 152–161.
[55] E. Peled, The electrochemical behavior of alkali and alkaline earth metals in nonaqueous battery systems—the solid electrolyte interphase model, J. Electrochem. Soc. 126 (1979) 2047–2051.
[56] H. Vogel, The law of the relationship between viscosity of liquids and the temperature, Phys. Z. 22 (1921) 645–646.
[57] V.G. Tamman, W. Hesse, Die Abhängigkeit der Viscosität von der Temperatur bie Unterkühlten Flüssigkeiten, Z. Anorg. Allg. Chem. 156 (1926) 245–257.
[58] G.S. Fulcher, Analysis of recent measurements of the viscosity of glasses, J. Am. Ceram. Soc. 8 (1925) 339–355.
[59] J.L. Souquet, M. Duclot, M. Levy, Salt-polymer complexes: strong or weak electrolytes? Solid State Ionics 85 (1996) 149–157.
[60] T.G. Fox, Influence of diluent and of copolymer composition on the glass temperature of a polymer system, Bull. Am. Phys. Soc. 1 (1956) 123–125.
[61] B. Lessard, M. Maric, Nitroxide-mediated synthesis of poly(poly(ethylene glycol) acrylate) (PPEGA) comb-like homopolymers and block copolymers, Macromolecules 41 (2008) 7870–7880.
[62] S. Sylla, J.-Y. Sanchez, M. Armand, Electrochemical study of linear and cross-linked POE-based polymer electrolytes, Electrochim. Acta 37 (1992) 1699–1701.
[63] L.J.A. Siqueira, M.C.C. Ribeiro, Molecular dynamics simulation of the polymer electrolyte poly(ethylene oxide)/LiClO4. I. Structural properties, J. Chem. Phys. 122 (2005) 194911.